Investigation of background edge thermal transport in ELMing and ELM-suppressed H-modes in DIII-D

W. M. Stacey, Georgia Tech, Atlanta, GA 30332
T. E. Evans, General Atomics, San Diego, CA 92186

August, 2006
Revised October, 2006

Abstract

Thermal diffusivities are inferred in the plasma edge of a matched pair of DIII-D [J. Luxon, Nucl. Fusion, 42, 614 (2002)] high confinement mode discharges, one with edge localized modes (ELMs) present and the other with ELMs suppressed by resonant magnetic perturbations. These experimentally inferred thermal diffusivity profiles are compared with the predictions of a variety of thermal transport theories.

PACS 52.55.Fi

I. Introduction

High performance (H-mode) plasmas in tokamaks are generally characterized by the cyclic buildup of the edge pressure pedestal until an edge localized MHD (magnetohydrodynamic) mode (ELM) of a few ms duration occurs, resulting in a sharp drop in the edge pressure pedestal and a large outflux of particles and energy into the scrape-off layer (SOL). Following the ELM event the pressure pedestal builds up over a period of typically tens of ms until the next ELM event occurs. References 1 and 2 review ELM behavior in tokamaks. The onset of ELMs is now reasonably well understood as being due to a combination ballooning-peeling (kink) mode MHD instability (e.g. Refs. 3-6).

Since ELMs limit the sustainable pedestal pressure they also limit the achievable central pressures in tokamaks with "stiff" temperature profiles, which could limit the performance of future tokamak reactors (see, e.g., Refs. 7 and 8). Furthermore, ELMs constitute a source of power pulses into the SOL and onto the divertor plates, which may overwhelm the heat removal capability in future tokamak reactors (see, e.g., Refs. 9 and 10).

These potential problems of ELMs have motivated an effort to suppress them by the addition of small resonant magnetic field perturbations (RMPs) that induce a chaotic behavior of the magnetic field lines[11-13], which should enhance the radial electron heat transport[14] and thereby reduce the edge pressure (gradient) below the threshold value for ELM instability. While this strategy has been successful in suppressing ELMs, there is evidence[15] suggestive that the reduction in edge pressure (gradient) is due to a reduction in the plasma density rather than to an increase in the electron thermal transport in the edge.

Our purpose in this paper is to investigate the thermal transport in H-mode discharges in which ELMs are suppressed by resonant magnetic perturbations in comparison to the 'background' thermal transport in ELMing H-mode discharges (transport in addition to the pulsed, large scale convective transport in the ELM event itself). For this purpose, we make use of a recently developed methodology[16] for inferring edge thermal transport that takes into account the spatial variation over the edge

region of both the total and convective heat fluxes for ions and electrons due to radiation, recycling neutrals and ion-electron collisional energy transfer and the temporal variation of these heat fluxes due to the intermittent ELM events.

II. Matching ELM-suppressed and ELMing H-mode discharges

In this study, a matched pair of lower single null diverted discharges were used to compare the thermal transport in plasmas with ELMs to that obtained during ELM suppression with resonant magnetic perturbation from the DIII-D I-coil[17]. These discharges have plasma currents of 1.5 MA, a toroidal magnetic field B_T = 2.0 T and were configured for strong pumping with the lower divertor cryopump. The temporal evolution of the electron pedestal density, temperature and collisionality are shown in Fig. 1 along with the global energy confinement time, normalized plasma beta and lower divertor D_α recycling. The pedestal and divertor ELM dynamics with and without the resonant magnetic perturbation along with the pedestal density, temperature and pressure profiles measured in these discharges are discussed in detail in ref. [17].

In order to investigate the underlying thermal transport in the ELMing H-mode, we chose two times in the ELMing H-mode discharge 123302 to analyze. With reference to the D_α signal shown in Fig. 2c and the pedestal electron pressure shown in Fig. 2d, at 2500 ms a series of ELMs has reduced the pedestal pressure to a local (in time) minimum and an ELM event has just ended; we will subsequently refer to this shot-time at which the transient effect of ELMs on the pedestal is maximum as "post-ELM". Similarly, at 2600 ms the pedestal pressure has recovered from the transient effect of previous ELMs as fully as possible because the next ELM is just about to occur; this shot-time at which the transient effect of ELMs on the pedestal is minimum will be referred to as "pre-ELM". We choose 2500 ms to analyze in the ELM-suppressed phase of discharge 123301 and refer to this shot-time as "I-coil" because the I-coil is used to cause the ELM suppression by producing resonant magnetic perturbations.

Fits of the experimental density and temperature profiles used for analysis of these shot-times are shown in Figs. 3 and 4. The effect of the ELM in flattening the density profile and reducing the edge pedestal is clear from comparison of the "pre-ELM" and "post-ELM" curves in Fig. 3. The overall density (see Fig. 2e) is reduced for the "I-coil" shot-time but so also is the edge density gradient shown in Fig. 3. The electron temperature profile in the edge is affected remarkably little by either the ELMs or the I-coils, as shown in Fig. 4. The ion temperature, on the other hand, is transiently reduced somewhat by the ELMs (compare the "pre-ELM" and "post-ELM" ion temperature profiles in Fig. 4) and is much larger in the lower density "I-coil" shot-time.

Our objective is to analyze these profiles to infer information about the underlying thermal transport processes and how they are affected by ELMs and the I-coil. To further characterize the discharges, it is useful to display these data also in terms of the profiles of collisionality, $\nu_{ei}^{*} \equiv \nu_{ei} qR/\upsilon_{the}\,\varepsilon^{3/2}$, and of gradient scale length ratios $\eta_{i,e} \equiv L_{ni,e} \Big/ L_{Ti,e} \equiv \left(\frac{1}{T_{i,e}}\frac{\partial T_{i,e}}{\partial r}\right) \Big/ \left(\frac{1}{n_{i,e}}\frac{\partial n_{i,e}}{\partial r}\right)$ shown in Figs. 5 and 6. Viewed like this, the edge conditions are seen to be quite different for the pre- and post-ELM stages of the ELMing H-mode discharge 123302 and different yet again for the ELM-suppressed discharge 123301, notwithstanding the similarity in global (other than density) and machine parameters.

III. Method for inferring experimental thermal transport

Following the development of Ref. 16, the total ion and electron radial heat fluxes consist of conductive and convective components

$$Q_{i,e} = n_{i,e} T_{i,e} \chi_{i,e} L_{Ti,e}^{-1} + \frac{5}{2} \Gamma_{i,e} T_{i,e} \qquad (1)$$

Thus, if $n_{i,e}, T_{i,e}$ and $L_{Ti,e}^{-1}$ are determined experimentally (e.g. as given in Figs. 3 and 4) and $Q_{i,e}$ and $\Gamma_{i,e}$ are calculated from heat and particle balances, the experimental $\chi_{i,e}$ profile can be evaluated from

$$\chi_{i,e}^{\exp}(r) = L_{Ti,e}(r)\left[\frac{Q_{i,e}(r)}{n_{i,e}(r)T_{i,e}(r)} - \frac{5}{2}\frac{\Gamma_{i,e}(r)}{n_{i,e}(r)}\right] \quad (2)$$

This inference of $\chi_{i,e}$ depends not only on the measured temperature and density profiles and the total heat flux $Q_{i,e}$ profiles, but also on the convective heat flux profiles.

Equation (2) assumes the conventional diffusive/convective model of thermal transport. We note that there have been studies of the possibility that avalanche-type phenomena may be involved in transport in the pedestal region. It would seem that avanche-type phenomena would produce an intermittent convective thermal transport that could be included in the present formulation with an appropriate time-averaging.

We use an integrated modeling code system[18] that performs i) particle and power balances on the core plasma to determine the net particle and heat fluxes outward across the separatrix, which are used as input to ii) an extended 2-point divertor model (with radiation and atomic physics) that calculates plasma densities and temperatures in the divertor and SOL and the ion flux incident on the divertor plate, which iii) is recycled as neutral molecules and atoms that are transported (2D) through the divertor region across the separatrix into the plasma edge region. Any sources of gas puffed neutrals and the charge-exchange neutrals incident on the wall are also similarly transported inward. This integrated code system is used to calculate the ion particle and total heat fluxes crossing the separatrix from the core into the SOL, the neutral flux crossing the separatrix from the SOL into the core, and the resulting radial distribution of neutral atoms in the edge plasma. The integrated model is normalized to match measured line-average density, measured energy confinement time and measured central and pedestal densities and temperatures by adjusting the neutral source, the confinement factor (H), and profile factors.

The atomic physics data are taken from Ref. [19] (with subsequent extensions to higher temperatures and a reduction in elastic scattering cross-sections by 25% to remove charge-exchange contributions), and the radiation emissivity is calculated from a fit to coronal equilibrium calculations (taking into account the effect of charge-exchange and recombination in the presence of recycling neutrals) based on the ADPAC data[20]. The

neutral recycling model has been checked against both Monte Carlo calculations and DIII-D neutrals measurements[21].

Using these fluxes crossing the separatrix calculated with the integrated model as separatrix boundary conditions, we can then integrate the plasma ion particle balance equation

$$\frac{\partial \Gamma}{\partial r} = -\frac{\partial n_i}{\partial t} + n_e n_o < \sigma \upsilon >_{ion} + S_{nb}, \qquad \Gamma\left(r_{sep}\right) = \Gamma_{sep}^{\exp} \tag{3}$$

inward from the separatrix across the edge region to determine the edge distributions of the particle flux, $\Gamma(r)$, where n_o is the density of recycling and gas fueling neutrals and S_{nb} is the source rate of plasma ions due to neutral beam (and pellet) injection. We can also integrate the heat balance equations

$$\frac{\partial Q_i}{\partial r} = -\frac{\partial}{\partial t}\left(\frac{3}{2} n_i T_i\right) + q_{nbi} - \frac{3}{2}(T_i - T_o^c) n_i n_o^c < \sigma \upsilon >_{cx+el} - q_{ie}, \quad Q_i\left(r_{sep}\right) = Q_{sepi}^{\exp} \tag{4a}$$

and

$$\frac{\partial Q_e}{dr} = -\frac{\partial}{\partial t}\left(\frac{3}{2} n_e T_e\right) + q_{nbe} + q_{ie} - n_e n_o < \sigma \upsilon >_{ion} E_{ion} - n_e n_z L_z, \quad Q_e\left(r_{sep}\right) = Q_{sepe}^{\exp} \tag{4b}$$

inward from the separatrix to determine the $Q_{i,e}(r)$ needed to evaluate the radial distribution of $\chi_{i,e}$ from Eq. (2). Here $q_{nbi,e}$ is the local neutral beam power deposition density, n_o is the recycling neutral density, n_o^c is the density of 'cold' recycling neutrals that have not yet collided inside the separatrix and $1.5T_o^c$ is their average energy, $q_{ie} \sim \left(T_i - T_e\right)/T_e^{1.5}$ is the ion-electron equilibration rate, $E_{ion}(T_e, n_e)$ is the ionization energy, n_z is the impurity (carbon) density, $L_z\left(T_e, n_o\right)$ is the impurity radiation emissivity, $< \sigma \upsilon >_{cx+el}\left(T_i\right)$ is the charge-exchange plus elastic scattering rate coefficient, and $< \sigma \upsilon >_{ion}\left(T_e, n_e\right)$ is the electron impact ionization rate coefficient.

The experimental $n_{e,z}$ and $T_{i,e}$ and the calculated neutral density are used to evaluate the terms in Eqs. (3) and (4), which are then integrated radially inward from the experimental separatrix boundary conditions for the particle and heat fluxes determined

as discussed above. We must at present estimate the split of Q_{sep} into Q_{sepi} and Q_{sepe}, but only a relative narrow range of choices yields physically reasonable results.

IV. Inference of edge thermal transport from measurements

A. Comparison of pre- and post-ELM stages of ELMing H-mode

The various heating and cooling terms appearing in Eqs. (4) were evaluated using the experimental density and temperature profiles shown in Figs. 3 and 4. The results are shown in Figs. 7 and 8 for the post-ELM stage at 2500 ms and the pre-ELM stage at 2600 ms, respectively, of shot 123302. The results of integrating these equations (and the continuity equation) subject to separatrix boundary conditions determined from global particle and power balances in an integrated code, as described in the previous section, are shown in Figs. 9 and 10. There is a substantial contribution of the time derivative terms in Eqs. (3) and (4) in the post-ELM stage at 2500 ms as the collapsed pedestal density and pressure recover from the ELM crash ($\frac{1}{n}\frac{\partial n}{\partial t} \approx \frac{1}{nT}\frac{\partial nT}{\partial t} \approx 36 s^{-1}$ determined from measured pedestal pressures), a substantial collisional transfer of energy from ions to electrons $\left(q_{ie}\right)$ in both stages which is somewhat larger in the post-ELM stage, and a substantial charge-exchange cooling of ions in both stages which is somewhat larger in the pre-ELM stage (see Figs. 7 and 8).

The total heat fluxes generally decrease with radius in the post-ELM stage because of the energy going into re-heating the edge plasma following the ELM crash, while in the pre-ELM stage the total heat fluxes generally increase with radius because the energy input from beam heating exceeds the losses and the rate of increase in internal energy is small (see Figs. 9 and 10). In both stages, the combination of collision and charge-exchange energy losses is greater than the beam heating for the ions just inside the separatrix, resulting in a drop in the ion total heat flux there. Conversely, the ion plus beam heating of the electrons is larger than the radiative and ionization cooling, resulting

in an increase of the electron total heat flux with radius over the entire edge in the pre-ELM phase where the energy content of the plasma is no longer increasing.

The convective heat fluxes tend to increase with radius because of the increase in $\Gamma(r)$ due to the ionization of recycling neutrals (calculated from the continuity equation), but tend to decrease with radius because of the decrease of $T(r)$ with radius. The increase due to neutral ionization predominates for the hotter ions, resulting in an ion convective heat flux that increases with radius just inside of the separatrix, but the stronger decrease in $T_e(r)$ with radius than in $T_i(r)$ results in a decreasing electron convective heat flux just inside the separatrix.

Using the total and convective heat fluxes shown in Figs. 9 and 10 and the experimental densities and temperatures shown in Figs. 3 and 4 to evaluate Eq. (2) yields the experimentally inferred thermal diffusivities shown in Fig. 11. Both $\chi_i^{\exp}$ and $\chi_e^{\exp}$ increase with time between ELMs, most strongly just inside the separatrix. Evidently, some transport mechanism(s) increases in strength as the pressure pedestal builds up between ELMs, but is suppressed by the ELM event. With reference to Figs. 3-6, the densities, collisionalities and gradient scale lengths differ significantly between the pre- and post-ELM stages, but the temperatures are very similar.

B. Comparison of ELM-suppressed and ELMing discharges

Figure 12 shows the heating and cooling terms in Eqs. (4) evaluated with the density and temperatures shown in Figs. 3 and 4 for the ELM-suppressed shot 123301 at 2500 ms. The lower plasma density for this shot than in the ELMing H-mode shot results in the charge-exchange cooling being larger and extending further into the plasma in this shot, but otherwise Fig. 12 is qualitatively similar to Figs. 7 and 8.

The heat fluxes resulting from solving Eqs. (4) and the continuity equation are shown for the ELM-suppressed shot in Fig. 13. The higher T_i in the ELM-suppressed shot results in the ion convective heat flux being a much more significant part of the total heat flux than in the ELMing shot; otherwise the heat fluxes in Fig. 13 are qualitatively

similar to the heat fluxes for the pre-ELM stage in Fig.10, neither of which are in a stage of rapid pedestal pressure increase.

Thermal diffusivities inferred by using the heat fluxes of Figs. 13 and the density and temperatures shown in Figs. 3 and 4 (for shot 123301) in Eq. (2) are shown in Figs. 14 and 15. The electron thermal diffusivity in the ELM-suppressed discharge is larger than that in the post-ELM stage of the ELMing discharge, as expected theoretically[14], but is remarkably similar to that in the pre-ELM stage of the ELMing discharge.

The ion thermal diffusivity in the ELM-suppressed discharge is also larger than in the post-ELM stage of the ELMing discharge, except for a dip in the former just inside the separatrix, and both decrease with radius. Either the resonant magnetic field or the reduced density seems to suppress the growth of some transport mechanism that causes the growth in χ_i^{exp} just inside the separatrix in the pre-ELM stage of the ELMing discharge, either directly or indirectly.

We note that neither the temperature distributions shown in Fig. 4 nor the inferred thermal diffusivities shown in Figs. 14 and 15 indicate the presence of a strong, localized "transport barrier". The ion temperature gradients are relatively uniform across the entire edge region and the electron temperature gradients without the I-coil are almost as uniform, and the inferred thermal diffusivities do not exhibit any strong localized "dip" coincident with a steep gradient region.

C. Consideration of uncertainties

Consideration of the uncertainty in the determination of the thermal diffusivities in Figs. 14 and 15 is in order at this point. With respect to Eq. (2), errors may enter the determination through the experimental density and temperature profiles or through the calculated total and convective heat fluxes. The error bars on the measured temperatures are < 10% and on the measured densities < 5%.

The possible errors in the calculated total and convective heat fluxes are probably primarily associated with the determination of the particle and heat fluxes crossing the separatrix (which are used as boundary conditions in the calculation of particle and heat flux distributions in the edge) and secondarily associated with the actual calculation of the particle and heat flux distributions from Eqs.(3) and (4). The total heat flux crossing the separatrix is determined from a power balance involving the known neutral beam

heating power plus the measured ohmic heating power less the measured radiation from inside the separatrix less the measured rate of increase in the total energy content of the plasma; the possible error in the total heat flux crossing the separatrix is probably < 10%. The split of this total heat flux crossing the separatrix between ions and electrons is not measured and must be estimated; however there is a rather narrow range of ion-electron splits for which the solution procedure described above yields physically reasonable results (convective heat flux less than total heat flux) over the entire edge region, as discussed in detail in Ref. 16. We used a 50:50 split and estimate (by calculation with other values of the split that lead to physically reasonable solutions) the maximum possible error in inferred thermal diffusivities associated with this uncertainty to be < 25% for the shots in this paper.

Aside from any error associated with determination of the separatrix boundary condition, any further error would arise from the calculation of the heating and cooling terms depicted in Figs. (7), (8) and (12). The use of a coronal equilibrium calculation for carbon line and recombination radiation is a possible source of error in the radiation cooling term, but this term is not a major contributor to the power balance. The calculation of the atomic physics terms depends on the calculation of the neutral influx, which is discussed below.

The particle flux crossing the separatrix (which is needed as a boundary condition in solving for the convective heat flux distribution) is determined from a particle balance on the plasma involving the known neutral beam particle source plus a calculated influx of neutral atoms minus the measured rate of increase of the average plasma density. The neutral influx is evaluated with a 2D transport calculation[21] with gas fueling and divertor and wall recycling sources represented explicitly. The wall recycling sources are adjusted so that the neutral influx fueling plus neutral beam fueling leads to a prediction of the average plasma density that matches the measured value when a "die-away" measurement of the particle confinement time is used, thus insuring that the correct neutral influx fueling rate is used in the calculation. As shown in Figs. (9), (10) and (13), the convective heat flux is typically 10-30% of the total heat, so that any error in the calculation of the convective heat flux is reduced by this factor in its contribution to error in the inferred thermal diffusivities.

Clearly, it is difficult to associate an 'error bar' with the inferred thermal diffusivities. However, the above considerations would suggest an uncertainty somewhere in the range of 25-100%.

V. Theoretical transport models

Now, we turn to the question of what mechanisms might be causing the observed transport. Although large-scale gyro-kinetic or gyro-fluid computer simulations of turbulent transport are becoming possible, such a calculation including the various atomic physics and other edge phenomena discussed above is probably beyond the present state-of-the art and is certainly well beyond the scope of this paper. Rather, we will compare the inferred thermal diffusivities against tractable theoretical formulas evaluated using the experimental data, with the intent of obtaining physical insight. However, some of the representations that we will employ are state-of-the-art for the particular transport mechanism (e.g. neoclassical and paleoclassical theories) and all of them are representative of forms used to represent that transport mechanism in present simulations.

A. Ion transport

1. Neoclassical

The neoclassical Chang-Hinton (neoch) expression for the ion thermal conductivity is[22,23]

$$\chi_i^{neoch} = \varepsilon^{1/2} \rho_{i\theta}^2 \nu_{ii} \left[a_1 g_1 + a_2 (g_1 - g_2 \right] \tag{5}$$

where the a's account for impurity, collisional and finite inverse aspect ratio effects and the g's account for the effect of the Shafranov shift

$$a_1 = \frac{0.66(1+154\alpha)+\left(1.88\sqrt{\varepsilon}-1.54\varepsilon\right)(1+3.75\alpha)}{1+1.03\sqrt{\mu_j^*}+0.31\mu_j^*}$$

$$a_2 = \frac{0.59\mu_j^*\varepsilon}{1+0.74\mu_j^*\varepsilon^{3/2}}\left[1+\frac{1.33\alpha(1+0.60\alpha)}{1+1.79\alpha}\right]$$

$$g_1 = \frac{1+\frac{3}{2}\left(\varepsilon^2+\varepsilon\Delta'\right)+\frac{3}{8}\varepsilon^3\Delta'}{1+\frac{1}{2}\varepsilon\Delta'} \qquad (6)$$

$$g_2 = \frac{\sqrt{1-\varepsilon^2}\left(1+\frac{\varepsilon\Delta'}{2}\right)}{1+\frac{\Delta'}{\varepsilon}\left(\sqrt{1-\varepsilon^2}-1\right)}$$

where $\alpha = n_I Z_I^2/n_i Z_i^2$, $\mu_i^* = \nu_{ii} qR/\varepsilon^{3/2} \upsilon_{thi}$ and $\Delta' = d\Delta/dr$, where Δ is the Shafranov shift. The impurity thermal conductivity is obtained by interchanging the i and I subscripts in the above expressions.

The Shafranov shift parameter may be evaluated from[24]

$$\Delta' \equiv \frac{d\Delta}{dr} = -\frac{1}{RB_\theta^2}\left(\frac{r^3}{a^2}\beta_\theta B_{\theta a}^2 + \frac{1}{r}\int_o^r B_\theta^2 r' dr'\right) \qquad (7)$$

where $\beta_\theta = p/(B_\theta^2/2\mu_0)$ and $B_{\theta a}$ denotes the poloidal magnetic field evaluated at $r = a$. Since we need this quantity at $r \approx a$, we can take advantage of the definition of the internal inductance

$$l_i = \frac{2\int_o^a B_\theta^2 r' dr'}{a^2 B_{\theta a}^2} \qquad (8)$$

where $\beta_{\theta a}$ denotes the quantity evaluated using the average pressure over the plasma and $B_{\theta a}$. Using a parabola-to-a-power current profile $j(r) = j_0(1 - (r^2/a^2))^v$, for which the ratio of the values of the safety factor at the edge to the center is $q_a/q_0 = v + 1$, and a fit[24]

$l_i = ln(1.65 + 0.89v)$ leads to the simple expression

$$\Delta' = -\frac{a}{R}\left(\bar{\beta}_{\theta a} + \frac{1}{2} l_i\right)$$
$$= -\frac{a}{R}\left(\bar{\beta}_{\theta a} + \frac{1}{2} ln\left(1.65 + 0.89\left(\frac{q_a}{q_o} - 1\right)\right)\right) \quad (9)$$

In the presence of a strong shear in the radial electric field, the particle banana orbits are squeezed, resulting in a reduction in the ion thermal conductivity by a factor of $S^{-3/2}$, where[25]

$$S = \left|1 - \rho_{i\theta}\left(\frac{d \ln E_r}{dr}\right)\left(\frac{E_r}{\upsilon_{thi} B_\theta}\right)\right| \quad (10)$$

Here $\rho_{i\theta}$ is the ion poloidal gyroradius.

The neoclassical transport phenomena are always present.

2. Ion temperature gradient modes

For a sufficiently large ion temperature gradient $\left(L_{Ti} \equiv -T_i/(dT_i/dr) < L_{Ti}^{crit} \simeq 0.1R \approx 0.18\right)$ the toroidal ion temperature gradient (itg) modes become unstable. As can be seen in Fig. 6, ITG modes are predicted to be unstable over the entire edge region for all shots considered. An estimate of the ion thermal conductivity due to itg modes is[26]

$$\chi_i^{itg} = \frac{5}{2}\left(\frac{1}{RL_{Ti}}\right)^{1/2}\left(\frac{T_e}{m_i}\right)\left(\frac{m_i}{e_i B}\right)\frac{1}{2}\rho_i \quad (11)$$

where ρ_i is the gyroradius in the toroidal magnetic field *B*, and $k_\perp \rho_i = 2$ has been used.

3. Drift Alfven modes

Drift Alfven (da) instabilities are driven by collisions and hence become important in the collisional edge plasma. Numerical modeling[27] indicates that ExB shear alone can not stabilize these modes (low collisionality and a steep pressure gradient are also needed). Figure 5 indicates that the collisionality is sufficiently large outside of $\rho \approx 0.97$ for da modes to be present. An analytical model[28] which takes these effects into account yields the expression

$$\chi_i^{da} = \chi_i^{gb} \bar{\bar{\chi}}_\perp\left(\beta_\parallel, \nu_n\right)/\sqrt{\mu} \quad (12)$$

where the ion gyro-Bohm thermal conductivity is $\chi_i^{gb} = \rho_s^2 c_s / L_{pi}$, with $L_{pi} \equiv -p_i/\left(dp_i/dr\right)$,

$$\mu = -k_{\|} L_{pi} \sqrt{m_i T_e / m_e T_i} \simeq \frac{L_{pi}}{qR} \sqrt{m_i T_e / m_e T_i} \tag{13}$$

for $k_{\|} \simeq 1/qR$, and

$$\overline{\overline{\chi}}_{\perp} = \left[\frac{\left(1+\beta_n^2\right)^{-3} + \nu_n^2}{1+\beta_n^2+\nu_n^{4/3}} \right] \tag{14}$$

where

$$\beta_n \equiv \left(\frac{m_i}{m_e}\right)^{1/2} \beta \frac{qR}{L_{pi}}, \quad \beta = \frac{n_e T_e}{B^2/2\mu_0}, \; \nu_n \equiv \left(\frac{m_i}{m_e}\right)^{1/4} \frac{\left(qRL_{pi}\right)^{1/2}}{\lambda_e} \tag{15}$$

with $\lambda_e = \upsilon_{the} / \nu_{ei}$ being the electron mean free path.

4. Thermal instabilities

In the weak ion-electron equilibration limit, local radial thermal instabilities in the edge ion and electron energy balances are decoupled, and the linear growth rates may be written in the general form[29]

$$\omega = -\frac{2}{3}\left(\chi_0 \left(\nu L_T^{-2} + k_r^2 \right) + \frac{5}{2} \nu \frac{\Gamma_{\perp}}{n} L_T^{-1} - \alpha \right) \tag{16}$$

where the first two terms represent the generally stabilizing effect of heat conduction and convection, respectively, with L_T^{-1} = (-dT/dr)/T for the species in question, $\Gamma_{\perp}$ being the ion or electron particle flux, and ν characterizing the temperature dependence of the underlying thermal conductivity for that species, $\chi_0 \sim T^{\nu}$. We used $\nu = 2.5$, but the results are relatively insensitive to this value. The α-terms represent the generally destabilizing atomic physics and impurity cooling terms in the respective growth rates for the ions

$$\alpha_i = \frac{5}{2}(\nu - 1)\nu_{ion} + \frac{3}{2}\nu_{at}^c \left(\nu - \left[1 + \frac{T_i}{\nu_{at}^c} \frac{\partial \nu_{at}^c}{\partial T_i} \right] \right) - \frac{1}{n}\left(\nu \frac{H_i}{T_i} - \frac{\partial H_i}{\partial T} \right) \tag{17a}$$

and for the electrons

$$\alpha_e = n_z \left(\frac{\nu L_z}{T_e} - \frac{\partial L_z}{\partial T_e} \right) + \nu_{ion} \left\{ \frac{5}{2}(\nu - 1) + \nu \frac{E_{ion}}{T_e} - \left(\frac{3}{2} + \frac{E_{ion}}{T_e} \right) \frac{T_e}{\nu_{ion}} \frac{\partial \nu_{ion}}{\partial T_e} \right\} - \frac{1}{n}\left(\nu \frac{H_e}{T_e} - \frac{\partial H_e}{\partial T_e} \right) \tag{17b}$$

The terms ν_{ion} and ν_{at} are the neutral ionization frequency in the pedestal region and the frequency of charge-exchange plus elastic scattering events involving 'cold' neutrals that have not previously undergone such an event in the pedestal region. E_{ion} is the ionization energy, and n_z and L_z are the density and radiative emissivity of impurities in the edge pedestal region. H represents any additional heating or cooling in the pedestal.

An estimate of the transport associated with such thermal instabilities (ti) is

$$\Delta\chi_{i,e}^{ti} \simeq \omega_{i,e} k_r^{-2} \tag{18}$$

In evaluating this expression we used $k_r = 5\ \mathrm{m}^{-1}$, corresponding to radial instabilities with wavelengths of 20 cm, which is about the maximum depth into the plasma that destabilizing neutral and/or impurity radiation effects might penetrate into a plasma. We used the neoclassical and paleoclassical values of the ion and electron thermal diffusivities to evaluate χ_0. When the calculated growth rate is negative, the thermal instabilities are not present and will not be shown.

B. Electron transport

1. Paleoclassical

A model based on classical electron heat conduction along field lines and magnetic field diffusion in which the electron temperature equilibrates within a distance L along the field lines and in which radially diffusing field lines carry this equilibrated temperature with them and thus induce a radial electron heat transport $M \simeq L/\pi qR \sim 10$ times larger than the resistive magnetic field diffusion rate leads to the following paleoclassical (paleo) expression for the electron heat diffusivity[30]

$$\chi_e^{paleo} = 1.5(1+M)\frac{\eta_{\|}^{nc}}{\eta_0}\nu_e\delta_e^2 \tag{19}$$

where taking L as the minimum of the electron collision mean free path and the maximum half length of the helical field results in

$$M = \min\{\ell_{\max}, \lambda_e\}/\pi Rq \tag{20}$$

where

$$\delta_e^2 \nu_e = \frac{1.4x10^3 Z_{eff}}{T_e^{3/2}(eV)}\left(\frac{\ln\Lambda}{17}\right), \quad \delta_e = c/\omega_{pe}, \ ,$$

$$\ell_{\max} \equiv \pi R q_* n_{\max} = \frac{\pi R q_*}{\left(\pi \bar{\delta}_e \frac{dq}{d\rho}\right)^{1/2}} = \frac{R\sqrt{\pi q}}{\left(\frac{\delta_e}{a}\left(\frac{1}{q}\frac{dq}{d\rho}\right)\right)^{1/2}},$$

$$\frac{\eta_{\parallel}^{nc}}{\eta_0} = \left[\frac{\sqrt{2}+Z_{eff}}{\sqrt{2}+13Z_{eff}/4}\right] + \left[\frac{\sqrt{2}+Z_{eff}-\ln(1+\sqrt{2})}{Z_{eff}\left(1+\nu_{*e}^{1/2}+\nu_{*e}\right)}\right]\frac{(1-f_c)}{f_c},$$

$$\nu_{*e} = Rq/\varepsilon^{3/2}\lambda_e, \ f_c = \frac{\left(1-\varepsilon^2\right)^{-1/2}(1-\varepsilon)^2}{1+1.46\varepsilon^{1/2}+0.2\varepsilon}, \ \lambda_e = \frac{1.2x10^{16}T_e^2(eV)}{n_e Z_{eff}}\left(\frac{17}{\ln\Lambda}\right) \tag{21}$$

The paleoclassical transport phenomena are always present.

2. Electron temperature gradient modes

The electron temperature gradient (etg) modes (electrostatic drift waves with $k_\perp c_s \le \omega_{pe}$) are unstable when $\eta_e \equiv L_n / L_{Te} \ge 1$, which is generally the case in the edge region for the shots considered in this paper, as shown in Fig. 6. An expression for the thermal conductivity due to the etg modes is given by[24]

$$\chi_e^{etg} = 0.13\left(\frac{c_s}{\omega_{pe}}\right)^2 \frac{\upsilon_{the} S_m}{qR}\eta_e(1+\eta_e) \tag{22}$$

where $S_m \equiv (r/q)(dq/dr)$ is the magnetic shear and ω_{pe} is the electron plasma frequency.

The cut-off for etg modes is given by[31]

$$\frac{R}{L_{Te}} < \text{larger}\left[\begin{array}{l} 0.8\, R/L_{ne}, or \\ \left(1+Z_{eff}T_e/T_i\right)\left(1.33+1.91r\frac{1}{q}\frac{dq}{dr}\right)(1-1.15\varepsilon)\end{array}\right] \tag{23}$$

3. Trapped Electron Modes

The principal electron drift instabilities with $k_\perp c_s \le \Omega_i$ arise from trapped particle effects when $\nu_e^* \equiv \nu_e / \left(\upsilon_{the}/qR\right)\varepsilon^{3/2} < 1$. In more collisional plasmas the mode becomes a collisional drift wave destabilized by passing particles. An expression for the electron thermal diffusivity that encompasses the dissipative trapped electron mode (tem) and the transition to the collisionless mode as $\nu_e^* \to 0$ is given by[24]

$$\chi_e^{tem} = 0.13\left(\frac{c_s}{\omega_{pe}}\right)^2 \frac{\upsilon_{the}\left(\frac{r}{q}\frac{dq}{dr}\right)}{qR}\eta_e\left(1+\eta_e\right) \tag{24}$$

The collisionality range encompassed by this expression indicates that tem modes should be present over the entire edge region for these shots.

4. Drift Resistive Ballooning Mode

The drift-resistive ballooning (drb) mode is destabilized by unfavorable curvature on the outboard side of the torus in a collisional edge plasma. Linear stability analysis[32] indicates that the transport associated with these modes can be characterized by a particle diffusion coefficient scaling $D \sim \left(2\pi q\right)^2 \rho_e^2 \nu_{ie}\left(R/L_n\right)$ and a proportionality constant equal to the flux surface average of the normalized fluctuating radial particle flux $\langle nV_r \rangle$. Subsequent calculations[33] found robust growth rates of drb's for the edge parameters of DIII-D and predicted the normalized fluctuating radial particle fluxes for models representative of TEXT and DIII-D core parameters $\langle nV_r \rangle \approx 0.01\text{-}0.05$. We adopt the form

$$\chi_e^{drb} = 4\frac{R}{L_n}\left(q\rho_e\right)^2 \nu_e \tag{25}$$

with the normalization factor equal to 4 to characterize the transport of electron energy due to drift-resistive ballooning modes, with the caveat that there could well be an additional normalization constant needed. We note that one group of transport modelers[31] calibrated this formula to L-mode data and found a factor of $94\kappa^{-4}$ (instead of 4) should multiply this expression (κ is the elongation), while another group[34] used this expression with the factor of 4.

5. Resonant Magnetic Perturbation Diffusion

A magnetic field line integration code[35] is used to numerically calculate the magnetic diffusivity D_m across the outer region of the plasma where resonant magnetic perturbations from the DIII-D I-coil are expected to produce a significant level of stochasticity. The magnetic diffusivity of a field line is defined as:

$$D_m = \delta r^2 / 2L \tag{26}$$

where δr is the total radial displacement, calculated at the outboard midplane, between the starting point of the field line calculation and its end point. Here, L is the total parallel field line length from the starting point to the end point. Since the DIII-D version of the field line integration code calculates trajectories in poloidal flux space (ψ), an average D_m^{ψ} taken over an ensemble of N starting points on a single flux surface is determined on each flux surface based on the diffusion field lines in flux space using:

$$\left\langle D_m^{\psi} \right\rangle = \frac{1}{N} \sum_{j=1}^{N} \delta\psi_j^2 \Big/ 2L_j \tag{27}$$

where $\delta\psi_j$ is the total displacement of a single field line in poloidal flux and L_j is its total parallel length. As discussed in Ref. [36], $\left\langle D_m^{\psi} \right\rangle$ is converted to real space variables $\left\langle D_m^{r} \right\rangle$ with units of meters using a geometric factor that accounts for the shape of the flux surface. Then, an average stochastic magnetic electron thermal diffusivity $\left\langle \chi_{e-m}^{r} \right\rangle$ in units of m^2/s is calculated using:

$$\left\langle \chi_{e-m}^{r} \right\rangle = \mathrm{v}_{the} \left\langle D_m^{r} \right\rangle \tag{28}$$

where v_{the} is the electron thermal speed on the starting flux surface. The code is typically set to calculate $N = 180$ poloidally distributed, equally spaced, field line trajectories on each flux surface and follows each field line until it either hits a solid surface or makes 200 toroidal revolutions. A field line escape fraction f_{esc}, the ratio of field lines hitting a solid surface to the number of field lines started on each flux surface N, is calculated on each flux surface and a weighted $\left\langle \chi_{e-m}^{r} \right\rangle_w$ is calculated using:

$$\left\langle \chi^r_{e-m} \right\rangle_w = f_{esc} \left\langle D^r_m \right\rangle \tag{29}$$

Values of f_{esc} and $\left\langle \chi^r_{e-m} \right\rangle$ calculated for discharge 123301 are given in refs. [17] and [36], respectively.

VI. Comparison of experimentally inferred and theoretical thermal diffusivities

The experimentally inferred electron thermal diffusivity (star symbol) is compared in Figs. 16-18 with the predictions of the various theoretical formulas of the previous section, evaluated using the experimental data of Figs. 3-5, for the post- and pre-ELM stages of the ELMing H-mode discharge and for the ELM-suppressed discharge. The inferred $\chi_e^{\exp}$ is in reasonable agreement with the paleoclassical prediction for both the ELM-suppressed discharge (Fig. 18) and the pre-ELM stage of the ELMing discharge (Fig. 17). The magnetic perturbation diffusion theory also is in reasonable agreement with $\chi_e^{\exp}$ for the ELM-suppressed discharge (Fig. 18). The resistive ballooning mode (rb) has the correct profile to account for the increase with radius just inside the separatrix, but a larger normalization constant than 4 would be needed to match experiment.

Predictions of the other theories have larger disagreement with the experimentally inferred $\chi_e^{\exp}$ profiles. The etg prediction is an order of magnitude too large. The tem prediction varies radially from strong under-prediction to strong over-prediction in two of the three cases. The predicted electron thermal instability growth rates were negative at all radii for all three cases, indicating no contribution to electron transport (however χ_0 was taken as the paleoclassical value, which may be inappropriate since the paleoclassical expression tends to over-predict the experimentally inferred $\chi_e^{\exp}$) .

Similarly, the inferred ion thermal diffusivity (star symbol) is compared with the predictions of the various theoretical formulas of the previous section in Figs. 19-21. There is good agreement with the itg prediction over almost the entire edge region except for a strong under-prediction just inside the separatrix. The criterion $\eta_i > 0.1R$ for the growth of toroidal itg modes has been used in plotting Figs. 19-21; if the more restrictive

criterion $\eta_i > 1$ was used the itg prediction would be zero in several other regions (see Fig. 6).

The other predictions of χ_i are generally in poorer agreement with $\chi_i^{\exp}$. Neoclassical theory (with S = 1) generally predicts χ_i profiles of similar shape as itg but an order of magnitude lower in value. The drift Alfven (da) χ_i generally increases with radius and becomes comparable to $\chi_i^{\exp}$ just inside the separatrix. The ion thermal instabilities have negative growth rates for the ELMing discharge, except just inside the separatrix at the pre-ELM stage where their estimated χ_i is comparable to the experimental value, and the ti prediction is not in good agreement with experiment for the ELM-suppressed discharge.

VI. Summary and conclusions

Thermal transport has been inferred from experimental temperature and density profiles and calculated conductive flux profiles (taking into account edge cooling due to atomic physics, ion-electron equilibration and convection) in the edge plasma for a matched pair of H-modes, one ELMing and the other with ELMs suppressed by resonant magnetic perturbations. The inferred thermal diffusivities were compared with the predictions of various theoretical models.

Both $\chi_i^{\exp}$ and $\chi_e^{\exp}$ increase with time between ELMs, most strongly just inside the separatrix. Evidently, some transport mechanism(s) increases in strength as the pedestal pressure builds up between ELMs, but is suppressed by the ELM event.

The resonant magnetic perturbations introduced by the I-coil do increase $\chi_e^{\exp}$ (relative to the background value without the I-coil just after the ELM crash), as predicted theoretically. Remarkably, this increased $\chi_e^{\exp}$ due to the I-coil is well matched over the entire edge region to the $\chi_e^{\exp}$ just before the ELM crash in the ELMing H-mode, which would seem to indicate that it is not the increase in $\chi_e^{\exp}$ caused by the resonant magnetic field perturbations that suppresses the ELMs. Rather, the resonant magnetic

perturbation seems to cause the discharge to operate at a lower average and pedestal density and thus at a pedestal pressure below the ELM threshold.

None of the theoretical predictions provides a good fit to the experimentally inferred thermal diffusivity over the entire edge region. The inferred $\chi_i^{\exp}$ profile agrees best with itg predictions, although there is a significant under-prediction just inside the separatrix for which there must be another explanation. The experimentally inferred $\chi_e^{\exp}$ agrees best with the paleoclassical and the magnetic perturbation predictions for the ELM-suppressed discharge and with the paleoclassical prediction just prior to the ELM crash in the ELMing discharge.

ACKNOWLEDGEMENTS: The authors are grateful to members of the DIII-D team who operated the experiment and measured and reduced the data discussed in this paper. The first author (WMS) is grateful to Glen Bateman, Jim Callen, Parvez Gudzar, and Alexie Pankin for discussion and clarification of certain aspects of the theoretical models and to General Atomics for their hospitality during the course of this work. The work was supported by the US Dept. of Energy through grant DE-FG02-99ER54538 with the Georgia Tech Research Corporation and contract DE-AC03-99ER54463 with General Atomics.

References

1. M. E. Fenstermacher, A. W. Leonard, P. B. Snyder, *et al*., Plasma Phys. Control Fusion, **45**, 1597 (2003).
2. N. Oyama, P. Gohil, L. D. Horton, et al., Plasma Phys. Control Fusion, **48**, A171 (2006).
3. R. L. Miller, Y. R. Lin-Liu, T. H. Osborne and T. S. Taylor, Plasma Phys. Control. Fusion, 40, 753 (1998).
4. J. W. Connor, R. J. Hastie, H. R. Wilson and R. L. Miller, Phys. Plasmas, 5, 2687 (1998).
5. H. R. Wilson and R. L. Miller, Phys. Plasmas, 6, 873 (1999).
6. P. B. Snyder, H. R. Wilson, J. R. Ferron, *et al*., Phys. Plasmas, 9, 2037, (2002); also Nucl. Fusion, 44, 320 (2004).
7. M. Kotschenreuther, W. Dorland, Q. P. Liu, *et al*., Proceedings of 16th Conference Plasma Physics and Controlled Fusion Research, Montreal, 1996 (IAEA, Vienna, 1997), Vol. 2, p 371.
8. J. E. Kinsey, R. E. Waltz and D. P. Schissel, Proceedings of 24th European Physical Society Conference, Berchtesgarten, 1997 (European Physical Society, Geneva, 1998) Vol. III, p 1081.
9. A. Loarte, G. Saibene, R. Sartori, et al., Plasma Phys. Control Fusion, **45**, 1549 (2003).
10. A. Loarte, G. Saibene, R. Sartori, et al., J. Nucl. Mater., 313-316, 962 (2003)
11. T. E. Evans, R. A. Moyer, P. R. Thomas, *et al*., Phys. Rev. Lett., **92**, 235003 (2004).
12. R. A. Moyer, T. E. Evans, T. H. Osborne, *et al*., Phys. Plasmas, **12**, 056119 (2005).
13. T. E. Evans, R. A. Moyer, J. G. Watkins, *et al*., Nucl. Fusion, **45**, 595 (2005).
14. A. B. Rechester and M. N. Rosenbluth, Phys. Rev. Lett., 40, 38 (1978).
15. T. E. Evans, R. A. Moyer, K. H. Burrell, *et al*., Nature Physics, 1, 419 (2006).
16. W. M. Stacey and R. J. Groebner, Phys. Plasmas, 13 (July, 2006).

17. T. E. Evans, K. H. Burrell, M. E. Fenstermacher, *et al*, Phys. Plasmas, 13, 056121 (2006).
18. W. M. Stacey, Phys. Plasmas, 5, 1015 (1998); also 8, 3673 (2001); also Nucl. Fusion, 40, 965 (2000).
19. W. M. Stacey, E. W. Thomas and T. M. Evans, Phys. Plasmas, 2, 3740 (1995); also 4, 678 (1997).
20. R. Hulse, Nucl. Technol./Fusion, 3, 259 (1983).
21. W. M. Stacey, Nucl. Fusion, 40, 965 (2000).
22. C. S. Chang and F. L. Hinton, Phys. Fluids, 25, 1493 (1982).
23. C. S. Chang and F. L. Hinton, Phys. Fluids, 29, 3314 (1986).
24. J. A. Wesson, *Tokamaks,* 2nd ed. (Clarendon Press, Oxford, 1997).
25. K. C. Shaing and R. D. Hazeltine, Phys. Fluids B, 4, 2547 (1992).
26. F. Romanelli, W. M. Tang and R. B. White, Nucl. Fusion, 26, 1515 (1986).
27. B. N. Rogers, et al., Phys. Rev. Lett., 81, 4396 (1998).
28. W. Kerner, Contrib. Plasma Phys., 38, 118 (1998).
29. W. M. Stacey, Phys. Plasmas, 6, 2452 (1999).
30. J. D. Callen, Nucl. Fusion, 45, 1120 (2005).
31. G. Bateman, A. H. Kritz, J. E. Kinsey, *et al*., Phys. Plasmas, 5, 1793 (1998).
32. D. R. McCarthy, P. N. Gudzar, J. F. Drake, *et al*., Phys. Fluids B, 4, 1846 (1992).
33. P. N. Gudzar, J. F. Drake, D. R. McCarthy, *et al.,* Phys. Fluids B, 5, 3712 (1993).
34. D. Kalupin, M. Z. Tokar, B. Unterberg, *et al*., Nucl. Fusion, 45, 468 (2005).
35. T.E. Evans, R.A. Moyer and P. Monat Phys. Plasmas **9**, 4957 (2002).
36. L. W. Yan and T. E. Evans, "Stochastic magnetic boundary modeling with large ELM suppression in a high confinement plasma in DIII-D", to appear in J. Nucl. Mater. (2006).

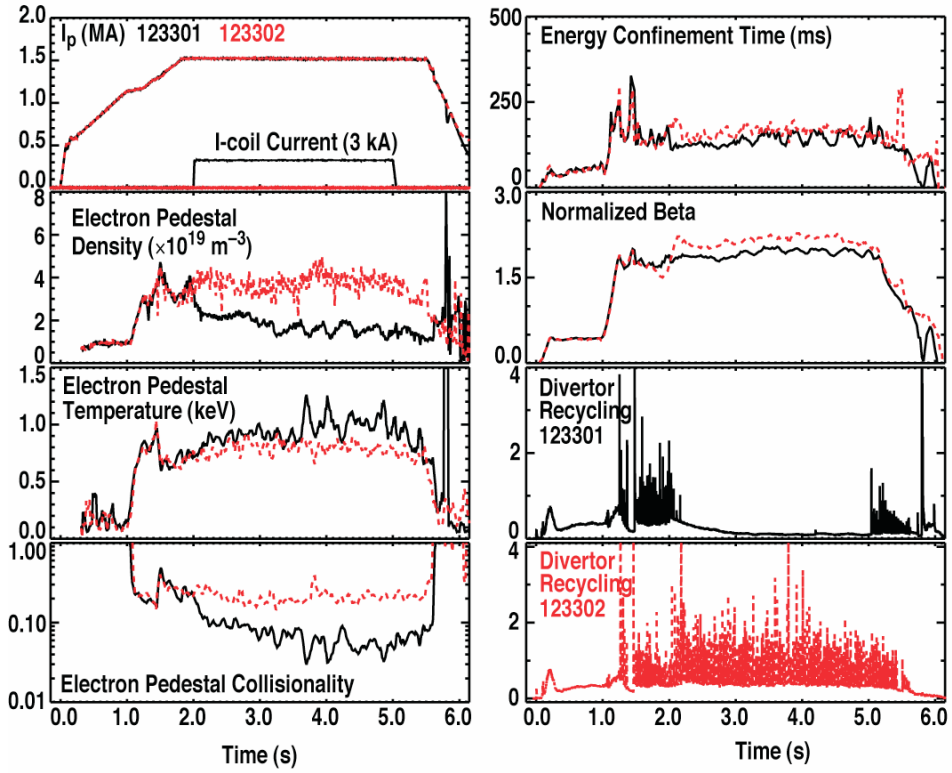

Figure 1. (Color online) Left column - top to bottom; Plasma and I-coil current, electron pedestal density, electron pedestal temperature, electron pedestal collisionality. Right column – top to bottom; energy confinement time, normalized plasma pressure (β_N), lower divertor D_α recycling for discharge 123301 and lower divertor D_α recycling for discharge 123302 as a function of time.

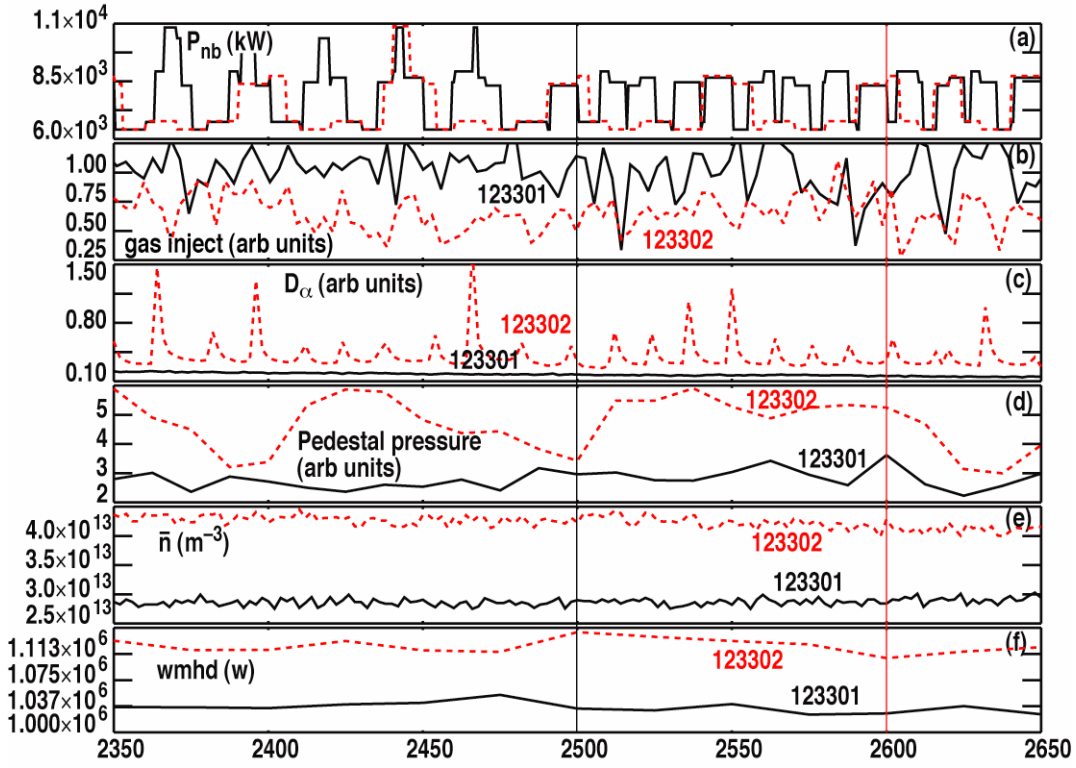

Figure 2. (Color online) Parameters for shots 123301 and 123302 over the interval 2350-2650 ms: a) injected beam power; b) injected gas fueling; c) D_α signal; d) pedestal electron pressure; e) line-average density; and f) global plasma energy content.

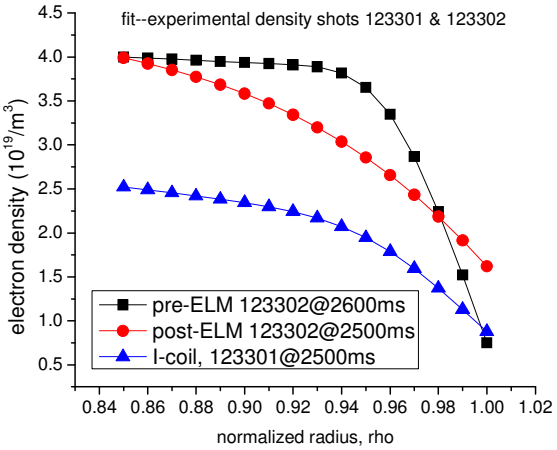

fig 3

Figure 3. (Color online) Fits to measured electron density distribution in DIII-D shots 123301 and 123302.

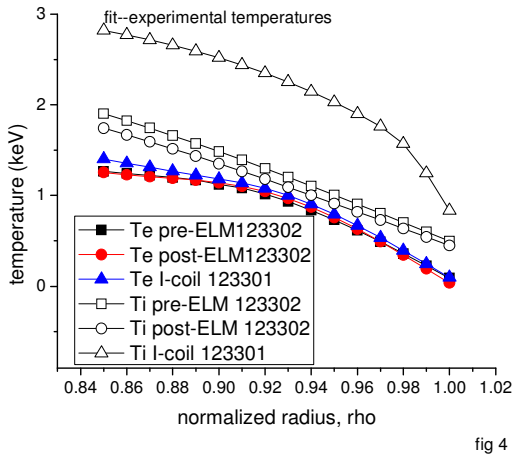

Figure 4. (Color online) Fits to measured temperature distributions in DIII-D shots 123301 and 123302.

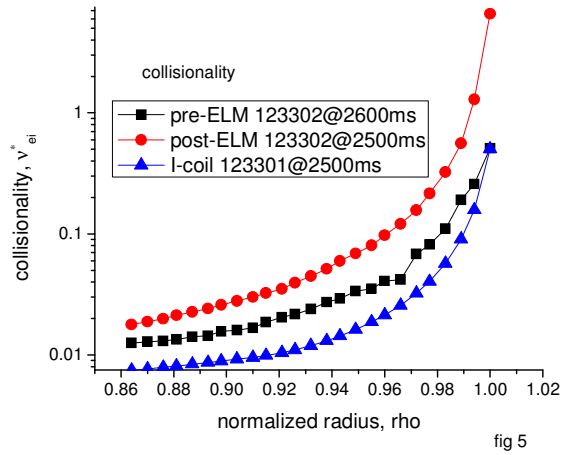

Figure 5. (Color online) Electron-ion collisionality parameter.

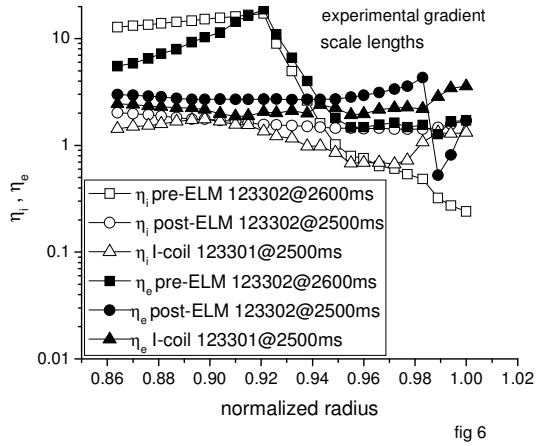

Figure 6. Gradient scale length ratio $\eta_{i,e} \equiv L_{ni,e} / L_{Ti,e}$.

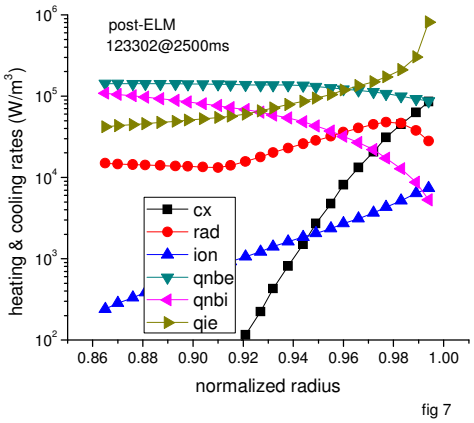

Figure 7. (Color online) Heating and cooling profiles at post-ELM time in shot 123302.

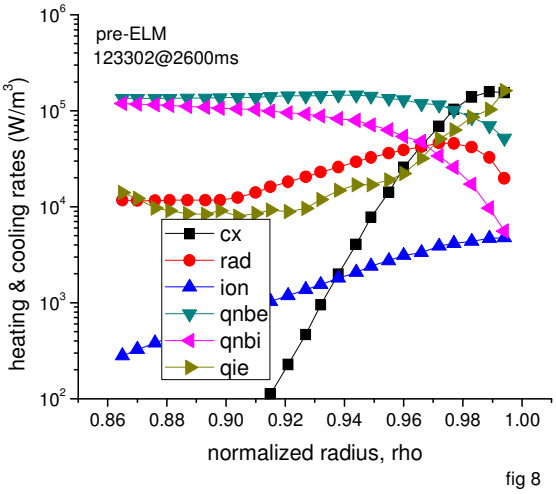

Figure 8. (Color online) Heating and cooling profiles at pre-ELM time in shot 123302.

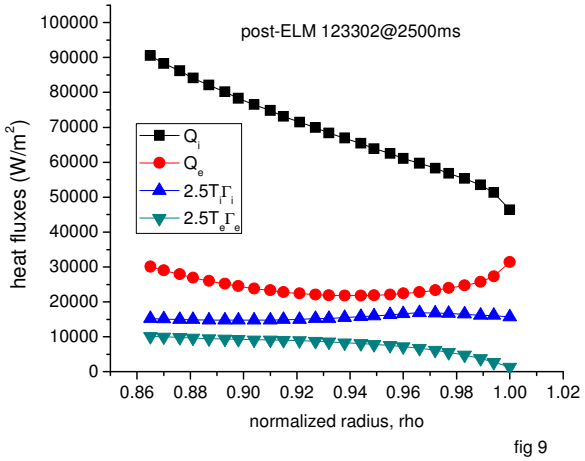

Figure 9. (Color online) Calculated total and convective heat fluxes at the post-ELM time in shot 123302.

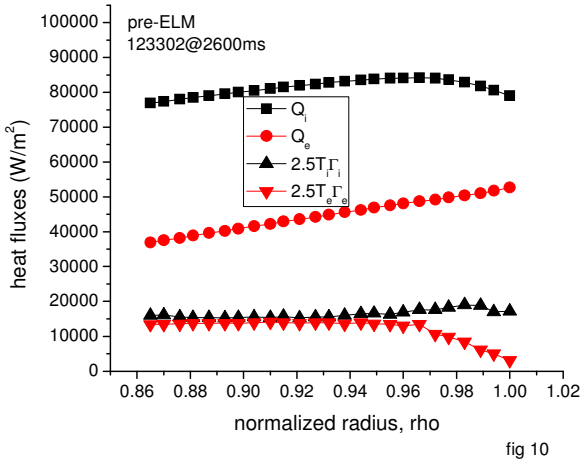

Figure 10. (Color online) Calculated total and convective heat fluxes at the pre-ELM time in shot 123302.

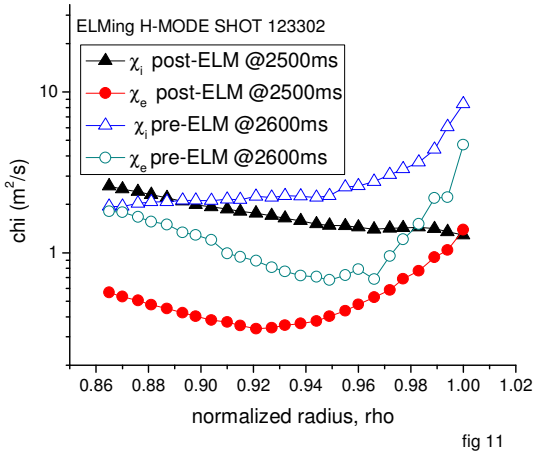

Figure 11. (Color online) Inferred experimental $\chi_{i,e}^{\exp}$ profiles in ELMing shot 123302.

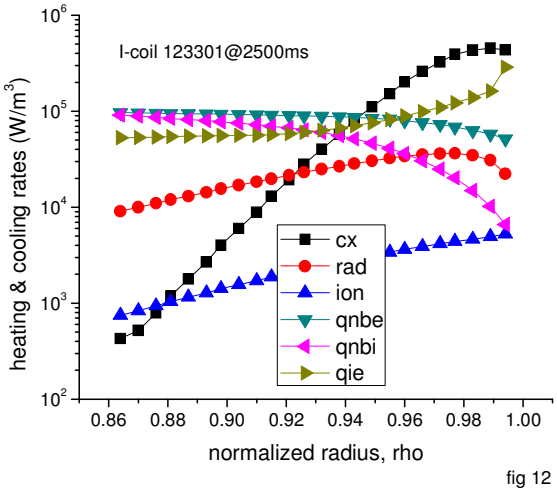

Figure 12. (Color online) Heating and cooling profiles in ELM-free shot 123302.

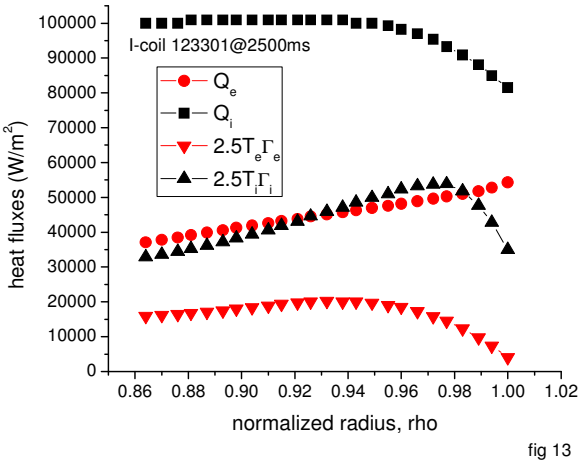

Figure 13. (Color online) Calculated total and convective heat fluxes in ELM-free shot 123301.

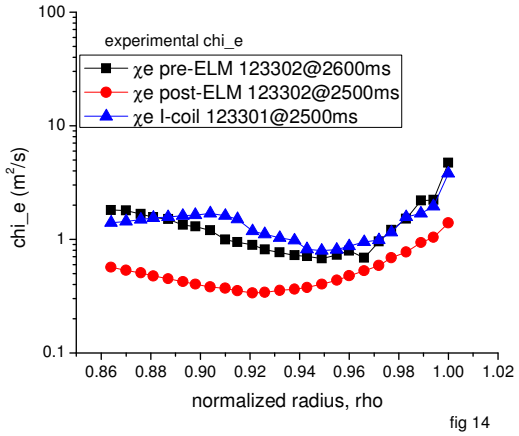

Figure 14. (Color online) Comparison of $\chi_e^{\exp}$ in ELMing and ELM-free shots.

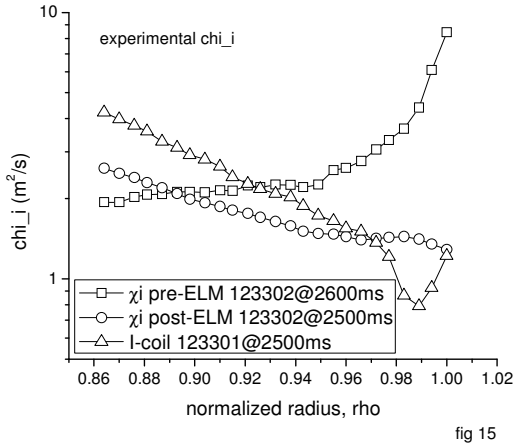

Figure 15. Comparison of $\chi_i^{\exp}$ in ELMing and ELM-free shots.

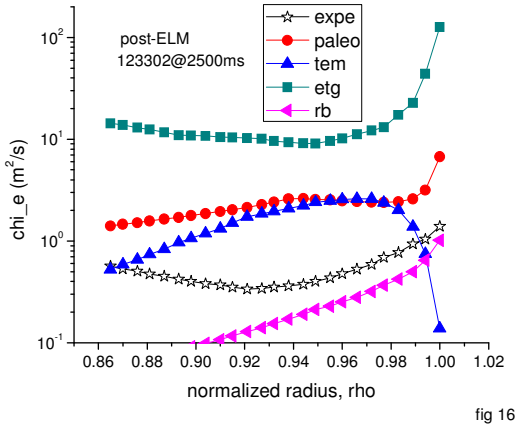

Figure 16. (Color online) Comparison of theoretical χ_e^{th} and experimentally inferred $\chi_e^{\exp}$ at the post-ELM time in shot 123302.

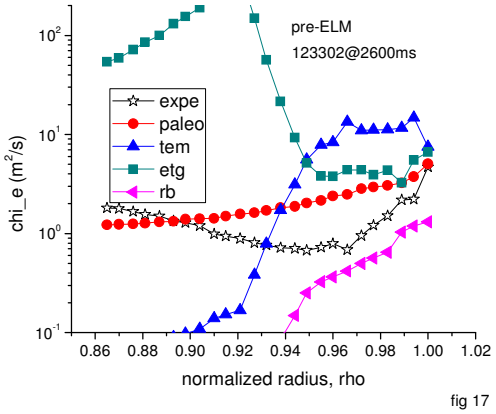

Figure 17. (Color online) Comparison of theoretical χ_e^{th} and experimentally inferred $\chi_e^{\exp}$ at the pre-ELM time in shot 123302.

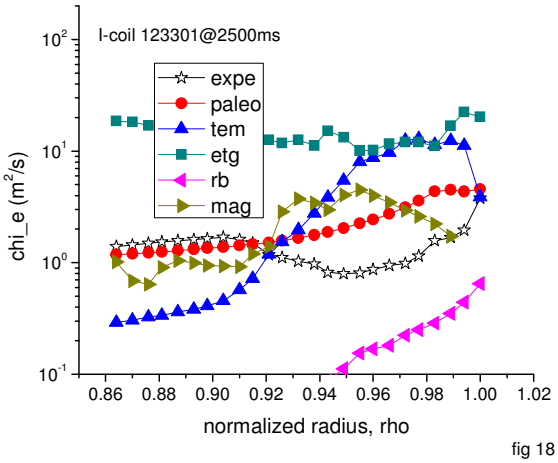

Figure 18. (Color online) Comparison of theoretical χ_e^{th} and experimentally inferred $\chi_e^{\exp}$ in ELM-free shot 123301.

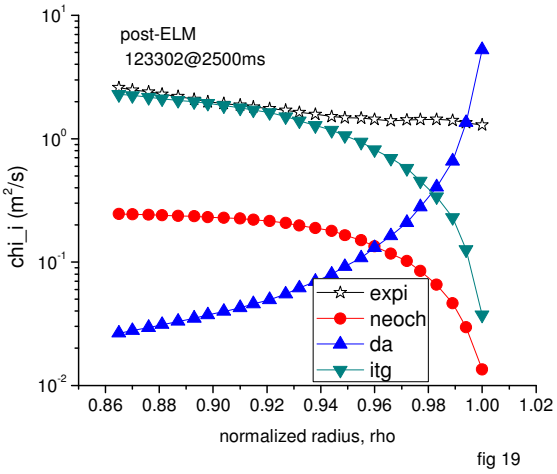

Figure 19. (Color online) Comparison of theoretical χ_i^{th} and experimentally inferred $\chi_i^{\exp}$ at the post-ELM time in shot 123302.

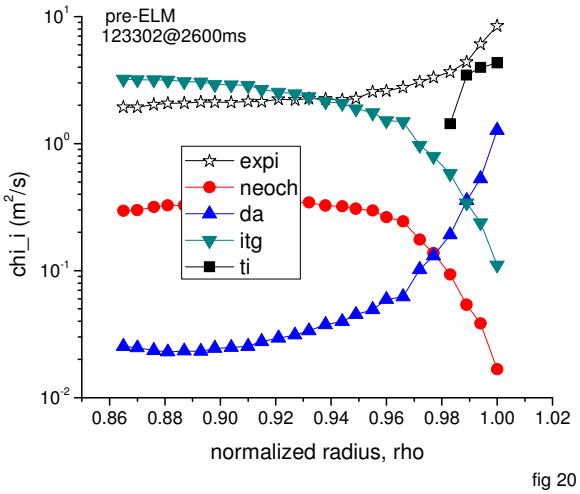

Figure 20. (Color online) Comparison of theoretical χ_i^{th} and experimentally inferred $\chi_i^{\exp}$ at the pre-ELM time in shot 123302.

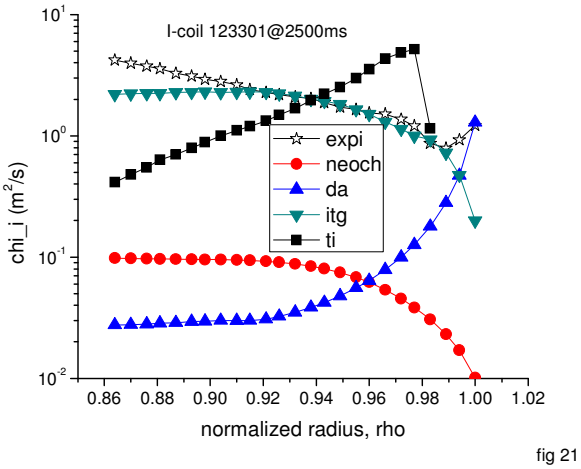

Figure 21. (Color online) Comparison of theoretical χ_i^{th} and experimentally inferred $\chi_i^{\exp}$ in the ELM-free shot 123301.